Helicase Assembly Protein Gp59 of Bacteriophage T4: Fluorescence Anisotropy and Sedimentation Studies of Complexes Formed with Derivatives of Gp32, the Phage ssDNA Binding Protein[†]

Hang Xu,[‡] Ying Wang,[‡] Jill S. Bleuit, and Scott W. Morrical*

Department of Biochemistry, Department of Microbiology and Molecular Genetics, and Vermont Cancer Center,
University of Vermont College of Medicine, Burlington, Vermont 05405

ABSTRACT: The gene 59 protein (gp59) of bacteriophage T4 performs a vital function in phage DNA replication by directing the assembly of gp41, the DNA helicase component of the T4 primosome, onto lagging strand ssDNA at nascent replication forks. The helicase assembly activity of gp59 is required for optimum efficiency of helicase acquisition by the replication fork during strand displacement DNA synthesis and is essential for helicase and primosome assembly during T4 recombination-dependent DNA replication transactions. Of central importance is the ability of gp59 to load the gp41 helicase onto ssDNA previously coated with cooperatively bound molecules of gp32, the T4 ssDNA binding protein. Gp59 heteroassociations with ssDNA, gp32, and gp41 all appear to be essential for this loading reaction. Previous studies demonstrated that a tripartite complex containing gp59 and gp32 simultaneously cooccupying ssDNA is an essential intermediate in gp59-dependent helicase loading; however, the biochemical and structural parameters of gp59−gp32 complexes with or without ssDNA are currently unknown. To better understand gp59−gp32 interactions, we performed fluorescence anisotropy and analytical ultracentrifugation experiments employing native or rhodamine-labeled gp59 species in combination with altered forms of gp32, allowing us to determine their binding parameters, shape parameters, and other hydrodynamic properties. Two truncated forms of gp32 were used: gp32-B, which lacks the N-terminal B-domain required for cooperative binding to ssDNA and for stable self-association, and A-domain fragment, which is the C-terminal peptide of gp32 lacking ssDNA binding ability. Results indicate that gp59 binds with high affinity to either gp32 derivative to form a 1:1 heterodimer. In both cases, heterodimer formation is accompanied by a conformational change in gp59 which correlates with decreased gp59−DNA binding affinity. Hydrodynamic modeling suggests an asymmetric prolate ellipsoid shape for gp59, consistent with its X-ray crystallographic structure, and this asymmetry appears to increase upon binding of gp32 derivatives. Implications of our findings for the structure and function of gp59 and gp59−gp32 complexes in T4 replication are discussed.

An early and crucial step in the initiation of DNA replication is the recruitment of a DNA helicase to reconstitute a processive replication fork. In the bacteriophage T4, the replicative helicase is gene 41 protein (gp41), a member of the ring-hexamer class of helicases (*1*). Gp41 assembles and translocates in a $5' \rightarrow 3'$ direction along the displaced, lagging strand ssDNA[1] of the T4 replication fork. Gp41 also interacts with the T4 primase, gp61, to reconstitute the phage primosome and so is essential for lagging strand DNA synthesis (reviewed in ref *2*). The recruitment of gp41, and thus of the primosome, to the lagging strand of the replication fork is limited by the helicase's intrinsically low affinity for ssDNA and by the saturation of the lagging strand ssDNA by gp32, the T4 ssDNA binding protein or ssb. Gp32, due to its abundance and to the high affinity and cooperativity of its ssDNA binding, inhibits helicase loading by competing with gp41 for ssDNA binding sites. A third phage-encoded protein, gp59, is required for efficient helicase loading at the replication fork (*3*).

Gp59 belongs to a class of proteins referred to as recombination/replication mediator proteins or RMPs, which were recently reviewed (*4*). Gp59 (26 kDa) is an adapter molecule with binding affinity for DNA (fork DNA > ssDNA > dsDNA), gp41 helicase, and gp32 ssb (*3, 5−7*). Gp59 binds cooperatively to ssDNA, and the degree of cooperativity is modulated by ions (*8*). The X-ray crystallographic structure of gp59 was determined recently (*7*). Gp59 crystallizes as a monomer and is asymmetric in

structure. It is comprised of two globular, largely α-helical domains separated by a hinge region. The two globular domains are referred to as the N- and C-domains after their proximity to the N- and C-terminal ends of the polypeptide, respectively. The precise locations of binding sites for DNA, gp41, and gp32 on the surface of gp59 remain to be determined experimentally.

Gp59–gp41 heteroprotein interactions modulate the enzymatic activities of the helicase and facilitate its assembly onto ssDNA in the presence or absence of gp32 (*3, 6, 9–13*). When gp32 saturates a ssDNA molecule, the gp59 requirement for helicase loading becomes virtually absolute (*6, 9*). During strand displacement DNA synthesis reactions, gp59 relieves a gp32 concentration-dependent time lag in the acquisition of gp41 helicase by nascent replication forks (*3*). Gp59 is essential for DNA replication initiated via the T4 recombination-dependent replication (RDR) pathway (reviewed in refs *14* and *15*). In this reaction, no lagging strand synthesis occurs in the absence of gp59 since access of gp41 to the lagging strand ssDNA is completely blocked by the combination of gp32 plus T4 homologous recombination proteins uvsX and uvsY (*16, 17;* J. Barry, M. L. Wong, and B. Alberts, manuscript in preparation). Gp41–ssDNA assembly in the presence of uvsX requires both gp59 and gp32, suggesting that gp59 targets helicase assembly onto patches of cooperatively bound gp32 interrupting uvsX–ssDNA presynaptic filaments (J. Barry, M. L. Wong, and B. Alberts, manuscript in preparation; *17*).

Gp59 exhibits a very strong and specific interaction with gp32 (*3, 5, 6, 9*). Gp32 (33.5 kDa) is comprised of three structurally and functionally defined domains (*18*): the N-terminal "B" or basic domain (residues 1–21) required for cooperativity and self-association; the "core domain" (residues 22–253) containing the ssDNA binding site and a structural Zn^{2+} atom; and the C-terminal "A" or acidic domain (residues 254–301), site of specific interactions with several T4 replication and recombination proteins. Morrical et al. (*9*) demonstrated that gp59 binds predominantly to the A-domain of gp32 and that the isolated A-domain fragment retains high-affinity interactions with gp59. The interaction of the A-domain with gp59 strongly modulates the ssDNA binding activity of gp59 (*10*). The interactions of other truncated forms of gp32 with gp59 have been investigated: Gp32-B, which lacks the B-domain but retains the intact core and A-domains, interacts strongly with gp59 (see Results). In contrast, gp32-A, which contains the intact B-domain and core domain but lacks the A-domain, exhibits very weak interactions with gp59 (*9; 34*).

Gp59–gp32 interactions play an essential role in gp59-mediated assembly of the gp41 helicase onto gp32-covered ssDNA. A tripartite gp59–gp32–ssDNA complex is required for helicase loading, whereas single-stranded DNA molecules covered with gp32-A are completely refractory to helicase assembly, even in the presence of gp59 (*9, 10*). There appears to be a critical cluster size of gp32 molecules bound contiguously to ssDNA which acts as the target for gp59-directed helicase assembly (*9, 10*). The similarity in the ssDNA binding site sizes of gp59 and gp32 (*8*), plus the ability of gp59 to cosaturate ssDNA with gp32 (*9, 10*), suggested that a 1:1 stoichiometric interaction of gp59 with gp32 molecules may be an important biochemical and structural feature of the helicase assembly intermediate.

However, the precise structure of the gp59–gp32–ssDNA intermediate is unknown, and the stoichiometry of gp59–gp32 binding has not been determined directly. To begin to resolve these issues, we have undertaken the current study to define stoichiometry and other solution parameters of gp59 complexes formed with gp32 fragments containing the A-domain. Our results, based on quantitative fluorescence anisotropy, sedimentation velocity, and sedimentation equilibrium measurements, indicate that gp59 forms extremely stable, heterodimeric complexes with gp32 derivatives containing the A-domain and provide new insights on the structure and conformational dynamics of gp59 and gp59–gp32 complexes.

EXPERIMENTAL PROCEDURES

Reagents and Buffers. Chemicals, biochemicals, and commercial enzymes were purchased from Sigma unless specifically noted in the text. All reagents were of analytical grade, and solutions were made with deionized, glass-distilled water. The rhodamine derivative tetramethylrhodamine-5-iodoacetamide (5-TMRIA) was purchased from Molecular Probes, Inc. Reaction buffer used in rhodamine labeling of gp59 contained 20 mM Tris-HCl, pH 7.4, 50 mM NaCl, and 0.2 mM EDTA. Buffers used in analytical ultracentrifugation studies included AU-50 buffer (20 mM Tris-HCl, pH 8.0, 50 mM NaCl, and 5 mM $MgCl_2$), and AU-300 buffer (same composition as AU-50 buffer except [NaCl] = 300 mM).

T4 Proteins. Purification and storage conditions for the T4 gp59 (26.0 kDa), gp32 (33.5 kDa), gp32-B (30.8 kDa), and A-domain (9.5 kDa) protein species were as previously described (*6, 9, 19–21*). The purity of each T4 protein stock used in this study was greater than 98% based on analysis of Coomassie Blue-stained SDS–polyacrylamide gels. The concentrations of gp59, gp32, and gp32-B were determined by the absorbance at 280 nm, using molar extinction coefficients of $3.94 \times 10^4 \, M^{-1} \, cm^{-1}$ for gp59 and $4.13 \times 10^4 \, M^{-1} \, cm^{-1}$ for gp32 and gp32-B, based on their respective amino acid sequences (*22*). The concentration of A-domain fragment was determined by spectrophotometric Bradford assay, using bovine serum albumin standards.

Rhodamine Labeling of Gp59. All steps were carried out in darkness. Gp59 (3.0 mg) was dialyzed against reaction buffer at 4 °C overnight. A fresh 20 mM stock of 5-TMRIA in DMSO was prepared. A 3-fold molar excess of 5-TMRIA was added to the gp59 solution with gentle shaking after the addition of each drop of reagent, and then the mixture was incubated overnight at 4 °C. Subsequently, 2% 2-mercaptoethanol was added to consume excess 5-TMRIA and also to break any disulfide bonds generated between gp59 molecules during the reaction (see Figure 1 below). The mixture was incubated at 4 °C for 1 h and then extensively dialyzed against AU-50 buffer or AU-300 buffer at 4 °C overnight. The labeling efficiency was determined by UV–visible wavelength scans according to manufacturer's instructions (Molecular Probes, Inc.). All scans (240–600 nm) were performed on a Hitachi U-2000 spectrophotometer at 20 °C. The molar extinction coefficient for gp59 at 550 nm and the molar extinction coefficients for 5-TMRIA at 280 and 550 nm were calculated empirically using known gp59 and 5-TMRIA concentration standards.

ATPase Assay. Coupled spectrophotometric assays for gp41-catalyzed ATP hydrolysis were performed as described

by Morrical et al. (*6*). The reaction mixtures contained 20 mM Tris−HOAc, pH 7.4, 10 mM Mg(OAc)$_2$, 90 mM KOAc, 6 units/mL pyruvate kinase, 6 units/mL lactate dehydrogenase, 2.3 mM phosphoenolpyruvate, 0.23 mM NADH, 10 μM (nucleotides) M13mp19 ssDNA, 2.5 mM ATP, 70 μg/mL gp32, 5 μg/mL gp41, and 6 μg/mL gp59 or rhodamine-gp59 (Rh-gp59). These conditions approximate V_{max} for the ATP substrate (*6*).

Fluorescence Anisotropy Measurements. The interaction between rhodamine-labeled gp59 (Rh-gp59) and gp32 derivatives was studied by monitoring changes in the steady-state fluorescence anisotropy of the Rh-gp59 species. All measurements were made in a PTI QuantaMaster luminescence spectrometer (Photon Technology International, South Brunswick, NJ) equipped with polarizers for the excitation and emission beams. All experiments were carried out in a 1 cm path-length cuvette at room temperature, with the bandpass of excitation and emission monochromators set at 5 and 16 nm, respectively. Steady-state fluorescence anisotropy was calculated according to the equations:

$$A = (I_{vv} - GI_{vh})/(I_{vv} + 2GI_{vh}) \tag{1}$$

$$G = I_{hv}/I_{hh} \tag{2}$$

where A is anisotropy, G is a correction factor for wavelength-dependent distortion, and I is the fluorescence intensity component (subscript referring to the vertical or horizontal positioning of the excitation and emission polarizers, respectively).

Conditions for binding assays were as follows: Both Rh-gp59 and gp32 derivatives were dialyzed against buffer containing 20 mM Tris-HCl (pH 8.1), 0.2 mM EDTA, 50 mM NaCl, and 2 mM 2-mercaptoethanol. After dialysis, proteins were quantified and mixed in the cuvette to form a solution containing 10 nM Rh-gp59 and various concentrations of gp32 derivatives. The anisotropies were calculated as described above from the fluorescence intensities obtained at an excitation wavelength of 535 nm and an emission wavelength of 573 nm. The binding stoichiometry, n, was estimated from the intersection of lines drawn through the descending and plateau regions of the anisotropy data. Alternatively, stoichiometry (n) and dissociation constant (K) parameters were estimated by globally fitting the anisotropy data to eq 3 (*23*), using Datafit 7.1 nonlinear regression software (Oakdale Engineering):

$$\alpha[\text{Rh-gp59}]_t = n[\text{gp32x}]_t\alpha/(1 - \alpha) - K \tag{3}$$

where [Rh-gp59]$_t$ and [gp32x]$_t$ are the total molar concentrations of Rh-gp59 and gp32 derivatives, respectively, and

$$\alpha = (A - A_{min})/(A_{max} - A_{min}) \tag{4}$$

is the fraction of free Rh-gp59 protein, A is the fluorescence anisotropy at a given [gp32x]$_t$, A_{max} is the initial anisotropy, and A_{min} is the anisotropy at saturation.

Analytical Ultracentrifugation Studies. All analytical ultracentrifugation experiments were conducted in a Beckman Optima XL-I instrument equipped with both absorbance and Rayleigh interference optics. Sedimentation velocity and equilibrium experiments were performed at 20 °C in either AU-50 buffer or AU-300 buffer. Experimental data were collected using both optical systems in parallel whenever possible. Data editing and analysis programs MATCH and WINNONLIN were downloaded from the University of Connecticut Biotechnology Center/National Analytical Ultracentrifugation Facility FTP site at http://vm.uconn.edu/~wwwbiotc/uaf.html. Data analysis programs SEDNTERP, DCDT, and ULTRASCAN were downloaded from the Reversible Associations in Structural and Molecular Biology (RASMB) FTP site at http://www.bbri.org/RASMB/rasmb.html. The program SEDNTERP was used to calculate the partial specific volume ($\bar{v}$) and predicted protomeric mass value of each protein species on the basis of its amino acid composition. Solution densities (ρ) and viscosities (η) were calculated from their chemical compositions using SEDNTERP.

(A) Sedimentation Velocity. Cells for sedimentation velocity experiments contained 12 mm double sector charcoal-filled Epon centerpieces and sapphire windows. A Beckman An60-Ti 4-hole rotor was used, and the rotor speed was 60 000 rpm. Buffer conditions for each experiment are noted in the text. Sedimentation velocity experiments involving the rhodamine conjugated form of gp59, Rh-gp59, were analyzed by the method of van Holde and Weischet (*24*) using the program ULTRASCAN. Data were collected using the absorbance optics system of the Optima XL-I, and the cells were scanned at 550 nm (absorbance maximum of tetramethylrhodamine). Sedimentation velocity experiments involving unconjugated protein were analyzed by the time derivative of the concentration profile, $g(s^*)$, method (*25*) using the program DCDT. Data were collected using the Rayleigh interference optical system of the Optima XL-I. Interference data were corrected for integral fringe shifts introduced during Fourier analysis. Sedimentation coefficients have been corrected to standard conditions (20 °C in water) denoted as $s_{20,w}$. All sedimentation coefficients are reported in units of Svedbergs (S), where $1\ S = 1 \times 10^{-13}$ s.

(B) Sedimentation Equilibrium. Sedimentation equilibrium experiments were conducted in the Optima XL-I instrument, using the method of Yphantis (*26*). Rotor and cell setup were as described above for velocity experiments. For experiments involving the rhodamine conjugate, Rh-gp59, the rotor speed was set at 30 000 rpm, and absorbance data were collected at 550 nm as an average of 10 measurements at each radial position in 0.001 cm increments. For other protein species the absorbance wavelength was 280 nm, and rotor speeds were selected so that $\sigma \approx 2-5$, where

$$\sigma = M(1 - \bar{v}\rho)\omega^2/RT \tag{5}$$

is the reduced apparent molecular weight. The program MATCH was used to evaluate each equilibrium by collecting successive scans taken 2 h apart and comparing each data set to the final scan. Equilibrium was achieved when RMS deviations did not change significantly between the final three data sets, taken over a period of at least 6 h. The data were edited to remove extraneous data outside of the sample column. The collected absorbance data were edited and analyzed using the program WINNONLIN. A global fit to σ at the 95% confidence interval was performed. Conversion from σ to molar molecular weight was performed using eq 5.

Estimation of the Maximal Sedimentation Coefficient and Hydrodynamic Shape Parameters. The estimation of the

maximal sedimentation coefficient and hydrodynamic shape parameters was performed using the program SEDNTERP (equations described in ref *27*). Experimental sedimentation coefficients were derived from the sedimentation velocity data. The mass, partial specific volume, density, and viscosity parameters were calculated as described above. The maximal sedimentation coefficient was calculated assuming the protein species as an anhydrous sphere (*28*). The equivalent radius (R_0 or R_p) and the minimal frictional coefficient (f_0 or f_p) were calculated from the protein sequence according to the equations:

$$R_0 = (3M_r\bar{v}/4\pi N_0)^{1/3} \tag{6}$$

$$R_p = (6.72 \times 10^{-9})M_r^{1/3} \tag{7}$$

$$f_0 = 6\pi\eta R_0 \tag{8}$$

$$f_p = 6\pi\eta R_p \tag{9}$$

where η is the standard viscosity of pure water at 20 °C. The maximal sedimentation coefficient was then calculated according to either eq 10 or 11, where

$$s_{max} = M(1 - \bar{v}\rho)/Nf_0 \tag{10}$$

$$s_{max} = M(1 - \bar{v}\rho)/Nf_p \tag{11}$$

The experimental sedimentation coefficient was used to calculate the frictional coefficient according to the Svedberg equation:

$$s = M(1 - \bar{v}\rho)/Nf \tag{12}$$

A prolate ellipsoid model was used to calculate the hydration and asymmetry estimates. The major axis/minor axis ratio (a/b) was determined using a power series approximation of tabulated data for a/b as a function of f/f_p. The values then were used to calculate the corresponding degree of hydration.

RESULTS

Rhodamine Labeling of Gp59. A rhodamine-labeled form of gp59, Rh-gp59, was generated for use in fluorescence anisotropy experiments and in certain sedimentation experiments. Tetramethylrhodamine-5-iodoacetamide (5-TMRIA), a thiol-reactive reagent, was used for covalent conjugation of the fluor to cysteine residue(s) in gp59. This probe has an absorbance maximum at 543 nm and a fluorescence emission maximum at 567 nm. There are two cysteine residues in gp59 (Cys42 and Cys215), and they are distant from each other in the X-ray structure of the protein (*7*). Cys42 is solvent exposed according to its position in the X-ray structure and thus should be accessible to thiol-reactive probes. Cys215 appears to be more buried in the hydrophobic core of the molecule despite its position near the extreme C-terminus of gp59 and thus may be less accessible to thiol-reactive probes. We expected that one molecule of gp59 would be labeled with one molecule of rhodamine covalently linked to Cys42. However, absorbance data (not shown) of the rhodamine-gp59 conjugate indicated a molar ratio of 1.4 rhodamine moieties incorporated per gp59 molecule, indicating that both cysteine residues were modified in some gp59
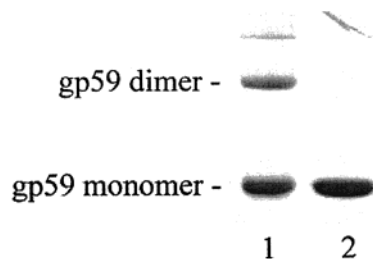

FIGURE 1: SDS−PAGE of rhodamine-labeled gp59. Lanes: 1, rhodamine-labeled gp59 (1.5 μg) prior to 1 h incubation with 2% 2-mercaptoethanol; 2, rhodamine-labeled gp59 (1.5 μg) after 1 h incubation with 2% 2-mercaptoethanol. Rhodamine labeling was performed as described in Experimental Procedures.

molecules. A possible explanation for this phenomenon is that the location of Cys215 near the extreme C-terminus of gp59 may allow its occasional exposure to solvent due to thermal motion of the C-terminal α-helix against the hydrophobic core.

The integrity of rhodamine-labeled gp59 was checked by SDS−PAGE. No degradation was observed, and the band of gp59 showed a pink color (prior to staining) due to the conjugated rhodamine. However, we noticed that there was another band on the gel with an apparent molecular weight twice that of gp59 (Figure 1). Since there was no visible contamination of the gp59 stock solution prior to rhodamine labeling, it is very likely that the new species is a covalently cross-linked product of two gp59 molecules. As an oxidant, 5-TMRIA could mediate the oxidation between cysteine residues on different gp59 molecules, allowing dimer formation via a covalent disulfide bridge. Another thin band appears at an even higher apparent molecular weight, possibly representing a trimer of gp59 (Figure 1). Our observation of gp59 cross-linking is consistent with reports that thiol cross-linking reagents can trap gp59 species up to pentameric in size (*34*). While the brief heating of the sample in SDS−PAGE gel loading buffer was not sufficient to break the disulfide bond, a treatment with 2% 2-mercaptoethanol for 1 h at 4 °C was sufficient to resolve the cross-links (Figure 1). The remaining 2-mercaptoethanol was removed from the solution by extensive dialysis. After this procedure, the rhodamine-labeled gp59 was found to be exclusively in the non-cross-linked form as determined by SDS−PAGE (Figure 1). This non-cross-linked Rh-gp59 species still retained approximately 1.4 rhodamine moieties per gp59 molecule as determined by absorbance measurements (data not shown).

The activity of the reduced, non-cross-linked stock of Rh-gp59 was tested by measuring its effects on the ssDNA-stimulated ATPase activity of the T4 gp41 DNA helicase. Gp59 is required for loading of gp41 helicase onto ssDNA saturated with the T4 gp32 ssb, resulting in a 20−25-fold stimulation of gp41's ATPase activity (*6*). The ATPase activity of gp41 in the presence of ssDNA, saturating gp32, and either Rh-gp59 or native gp59 was determined by a coupled spectrophotometric assay performed under V_{max} conditions with respect to ATP concentration. Under these conditions, V_{max} for the gp41-catalyzed ATP hydrolytic reaction was 6.8 nmol/(min·μg of protein) in the presence of native gp59, vs a comparable 6.2 nmol/(min·μg of protein) in the presence of Rh-gp59. This result indicates that Rh-gp59 retains native gp59's helicase loading and stimulation

Titration of Rh-Gp59 (10nM) with Gp32-B

EX=535 nm, EM=573 nm

n=1.1

[Gp32-B] (nM)

Titration of Rh-Gp59 (10nM) with Gp32 A domain

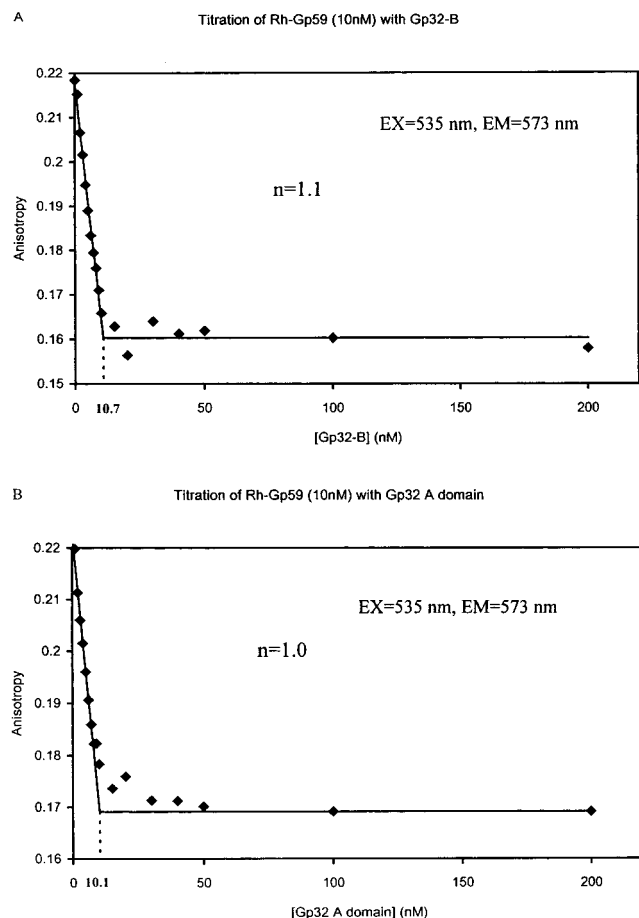EX=535 nm, EM=573 nm

n=1.0

[Gp32 A domain] (nM)

FIGURE 2: Fluorescence anisotropy titrations of Rh-gp59 with gp32 derivatives: calculation of binding stoichiometries and dissociation constants. Experimental conditions, fluorometer settings, and treatment of data were as described in Experimental Procedures. In each titration, the starting concentration of Rh-gp59 was 10 nM. (A) Titration of Rh-gp59 with gp32-B. (B) Titration of Rh-gp59 with gp32 A-domain fragment. Values of the n (stoichiometry) parameter were calculated from the intersections of asymptotic lines drawn through the descending and plateau regions of the data as shown.

functions without significant loss of activity. The ability of Rh-gp59 to perform these functions normally implies normal interactions of this species with gp41, gp32, and ssDNA (*6, 9*).

Stoichiometric Interaction of Rh-gp59 with Gp32 Derivatives. Changes in the steady-state fluorescence anisotropy of Rh-gp59 were used to monitor titrations of this conjugated species with the gp32 truncation derivatives gp32-B and A-domain, allowing the determination of binding parameters for the resulting complexes. Solution analyses of gp59 interactions with wild-type gp32 are complicated by several factors including gp32 self-association (see below) and the tendency of these two proteins to coprecipitate when mixed at micromolar concentrations (unpublished results). Both problems are at least partially alleviated by using either the gp32-B or A-domain fragments, both of which interact with gp59, lack significant self-association, and exhibit reduced tendencies to coprecipitate with gp59 (*9, 20*; unpublished observations).

Results of a fluorescence anisotropy titration of Rh-gp59 with gp32-B are shown in Figure 2A. A similar titration of Rh-gp59 with A-domain is shown in Figure 2B. In both cases, fluorescence anisotropy decreased sharply from an

initial value of $A_{max} = 0.22$ to a saturated value of $A_{min} \approx 0.16$ (Figure 2). The anisotropy decrease may be indicative of a conformational change in Rh-gp59, induced by binding of a gp32 derivative, that increases the mobility of one or more of the rhodamine labels (see Discussion). Binding stoichiometries were estimated empirically from the intersection of asymptotes as shown in Figure 2. The results demonstrate that both gp32-B and A-domain species bind to Rh-gp59 with a 1:1 stoichiometry. Additionally, the nearly identical decreases in steady-state fluorescence anisotropy observed in Figure 2 indicate that the binding of either gp32 species affects the conformation of Rh-gp59 in a very similar way.

By inspection, the data in Figure 2 are consistent with very tight binding of the gp32 derivatives to Rh-gp59, with an upper limit dissociation constant in the low nanomolar range. This conclusion is supported by results obtained from global nonlinear regression fits of the data in panels A and B of Figure 2, respectively, to eq 3 (data not shown). In the case of the A-domain fragment, this treatment yielded a stoichiometry parameter of $n = 0.9 \pm 0.1$ and a dissociation constant of $K = 2 \pm 1$ nM with an R^2 value of 0.99. For gp32-B the parameters were $n = 1.4 \pm 0.4$ and $K = 3 \pm 2$ nM with $R^2 = 0.97$.

Fluorescence anisotropy gives a clear indication of the 1:1 binding stoichiometry and strong affinity of gp32 derivatives for gp59; however, it leaves unanswered the question of the oligomeric states of these complexes. The 1:1 complexes of gp59 and either gp32 derivative could take the form of $\alpha\beta$ heterodimers, $\alpha_2\beta_2$ heterotetramers, or even higher ordered mixed oligomers. This issue is resolved by sedimentation studies employing the analytical ultracentrifuge, as described in the following sections.

Oligomeric Structures of Gp59, Gp32, and Derivatives. Table 1A lists the experimentally determined sedimentation coefficients and apparent masses of the gp59, Rh-gp59, gp32, gp32-B, and gp32 A-domain protein species, as measured by velocity and equilibrium analytical ultracentrifugation. Also listed for comparison are the calculated protomer mass, partial specific volume, and predicted maximum sedimentation coefficient parameters for each protein species, derived from their respective amino acid sequences. Predicted maximum sedimentation coefficients were calculated using the program SEDNTERP, assuming that each species is monomeric in solution and behaves as an anhydrous sphere (*27, 28*).

The time derivative of the sedimentation velocity profile, $g(s^*)$, was used to determine the values of $s_{20,w}$ for the gp59, gp32, gp32-B, and A-domain protein species (*25*). Simple Gaussian-shaped curves were obtained in all cases for the gp59, gp32-B, and A-domain species (data not shown), yielding corresponding $s_{20,w}$ values of 2.5, 2.5, and 0.8 S, respectively. The $s_{20,w}$ values of gp59 and A-domain were independent of concentration and were smaller than their calculated protomeric s_{max} values, indicating that these species likely behave as monomers in solution. This is confirmed by sedimentation equilibrium data which also indicate monomeric solution structures for gp59 and A-domain (Table 1A). The monomeric structure of gp59 determined here is consistent with its crystal structure and with previous data from sucrose gradients (*5, 7*). The sedimentation coefficient of gp32-B was concentration

Table 1: Calculated and Experimental Sedimentation Parameters of the T4 Gp59 and Gp32 Proteins and Their Derivatives and Complexes[a]

A	protein/ derivative	calcd protomeric mass (kDa)[b]	calcd $\bar{v}$ (cm³/g)[b]	exptl mass, M_{app} (kDa)[c]	calcd s_{max} of protomer[d]	exptl $s_{20,w}$ (S)[e]	velocity method[f]
	gp59	26.0	0.748	27.8 ± 2.2	2.91	2.5	$g(s^*)$
	Rh-gp59	26.4	0.748[b]	26.6 ± 0.8	3.15	2.25	VHW
	gp32	33.5	0.726	ND	3.74	≤7.5[g]	$g(s^*)$
	gp32-B	30.8	0.725	27.0 ± 2.1	3.58	2.5−2.8[g]	$g(s^*)$
	A-domain	9.5	0.716	9.2 ± 0.8	1.68	0.8	$g(s^*)$

B	protein complex	calcd mass of $\alpha\beta$ dimer (kDa)[b]	calcd $\bar{v}$ of $\alpha\beta$ dimer (cm³/g)[b]	exptl mass, M_{app} (kDa)[c]	calcd s_{max} of $\alpha\beta$ dimer[d]	exptl $s_{20,w}$ (S)[e]	velocity method[f]
	gp59−gp32-B	57.2	0.735	ND	5.14	3.5	$g(s^*)$
	Rh-gp59−A-domain	35.5	0.739	37.2 ± 1.7	3.71	2.75	VHW

[a] Methods and conditions for sedimentation velocity and equilibrium experiments are described in Experimental Procedures and in the text. Experiments involving protein species gp59, gp32, and gp32-B were conducted in low-salt AU-50 buffer containing 50 mM NaCl. Experiments involving Rh-gp59 and A-domain were conducted in AU-300 buffer containing 300 mM NaCl. [b] Predicted mass and $\bar{v}$ parameters of (A) individual protomeric species and (B) heterodimeric complexes were calculated from the amino acid composition of the protein or complex as described in Experimental Procedures. For the rhodamine-conjugated form of gp59, Rh-gp59, the value of $\bar{v}$ was assumed to be identical to that of unmodified gp59. [c] Experimentally measured apparent masses of individual proteins and of protein complexes were obtained by sedimentation equilibrium as described in Experimental Procedures. All listed values of M_{app} except that for gp32-B represent data obtained from fits of experimental data to ideal single component models. In the case of gp32-B, the data were best described by a nonideal model allowing weak dimerization ($K_a \approx 10$ M⁻¹). [d] Calculated maximum sedimentation coefficients of (A) individual protomeric species and (B) heterodimeric complexes were derived from the calculated mass and $\bar{v}$ parameters as described in Experimental Procedures. An anhydrous sphere is assumed for each protein or protein complex. [e] Experimentally measured sedimentation coefficients, corrected for 20 °C in water, were obtained by sedimentation velocity methods as described in Experimental Procedures and in the text. [f] The sedimentation velocity method was used to measure the sedimentation coefficient of a given protein species or complex. $g(s^*)$ denotes the time derivative method of Stafford (*25*); VHW denotes the van Holde−Weischet method (*24*). See Experimental Procedures for details. [g] Protein species displaying concentration dependence of $s_{20,w}$.

dependent: doubling the loading concentration from 10 to 20 μM increased the measured value of $s_{20,w}$ from 2.5 to 2.8 S. This increase appears to be the result of weak dimerization on the part of gp32-B, since sedimentation equilibrium gradients are fit optimally by assuming a weak monomer−dimer equilibrium ($K_a \approx 10$ M⁻¹) (Table 1A). Gp32-B was previously reported to be monomeric in solution; however, this result was based on a gel permeation chromatography method that likely would not have detected this very weak interaction (*20*).

The time derivative of sedimentation velocity was also used to analyze the oligomeric structure of full-length gp32 in solution. As reported in Table 1A, gp32's $s_{20,w}$ value is concentration dependent, and the corresponding $g(s^*)$ plots are not simple Gaussian-shaped curves (data not shown), indicating a distribution of sedimenting species. The highest $s_{20,w}$ values observed, approximately 7.5 S, suggest a dimeric or larger form of gp32. The sedimentation behavior of full-length gp32 is consistent with the known self-association properties of this protein (*20, 29, 30*).

The sedimentation properties of the rhodamine conjugated form of gp59, Rh-gp59, were analyzed by both velocity and equilibrium methods. Sedimentation parameters are summarized in Table 1A. Velocity data were analyzed by the method of van Holde and Weischet (*24*), while detecting Rh-gp59 by the absorbance of the rhodamine tag at 550 nm (Figure 3A,B). Rhodamine absorbance was also used to detect Rh-gp59 during equilibrium runs (see Figure 5). The velocity data replotted in terms of $s_{20,w}$ vs reciprocal square root of time (Figure 3B) show a reasonable convergence to a single $s_{20,w}$ value, although some concentration dependence of $s_{20,w}$ is evident. The integral distribution plot (Figure 4, filled circles) derived from the data in Figure 3A,B reflects this concentration dependence of $s_{20,w}$ as a positive slope in the near-vertical line. The median $s_{20,w}$ value of 2.25 for Rh-

gp59 is in reasonable agreement with the value of 2.5 measured for native gp59 by another method (Table 1A) and is consistent with a monomeric solution structure for Rh-gp59. The latter point is confirmed by sedimentation equilibrium data (Figure 5A; Table 1A), wherein the data are fit optimally by an ideal single component model yielding an apparent mass of 26.6 kDa, which is within 0.8% of the calculated protomeric mass of Rh-gp59.

Gp59 Forms Heterodimers with Gp32 Derivatives in Solution. The sedimentation properties of Rh-gp59 complexed with the A-domain fragment of gp32 were analyzed by both velocity and equilibrium methods. Sedimentation parameters are summarized in Table 1B. Velocity data were analyzed as described above for Rh-gp59 alone and are shown in Figure 3C,D. Note that by monitoring the absorbance of the rhodamine tag, we were able to perform these experiments in the presence of excess A-domain while measuring its effects on the sedimentation behavior of the gp59 component. In these experiments with Rh-gp59 plus excess A-domain, plots of $s_{20,w}$ vs reciprocal square root of time (Figure 3D) and of integral distribution of $s_{20,w}$ (Figure 4, filled squares) both indicate a reasonable convergence to a single $s_{20,w}$ value, although limited concentration dependence is still evident. The degree of concentration dependence is similar to that observed in the experiment with Rh-gp59 alone (Figure 3B; Figure 4, filled circles). The data suggest that the Rh-gp59−A-domain complex sediments as a single species with a median $s_{20,w}$ value of 2.75, which is an increase of 0.5 S over Rh-gp59 alone (Table 1B). There is no indication of a 2.25 S species in the sample, indicating that all Rh-gp59 exists in a complex with A-domain under these conditions. The $s_{20,w}$ value of 2.75 S for Rh-gp59−A-domain is consistent with a heterodimeric solution structure for this complex, given its calculated s_{max} value of 3.71. The existence of the Rh-gp59−A-domain heterodimer is con-
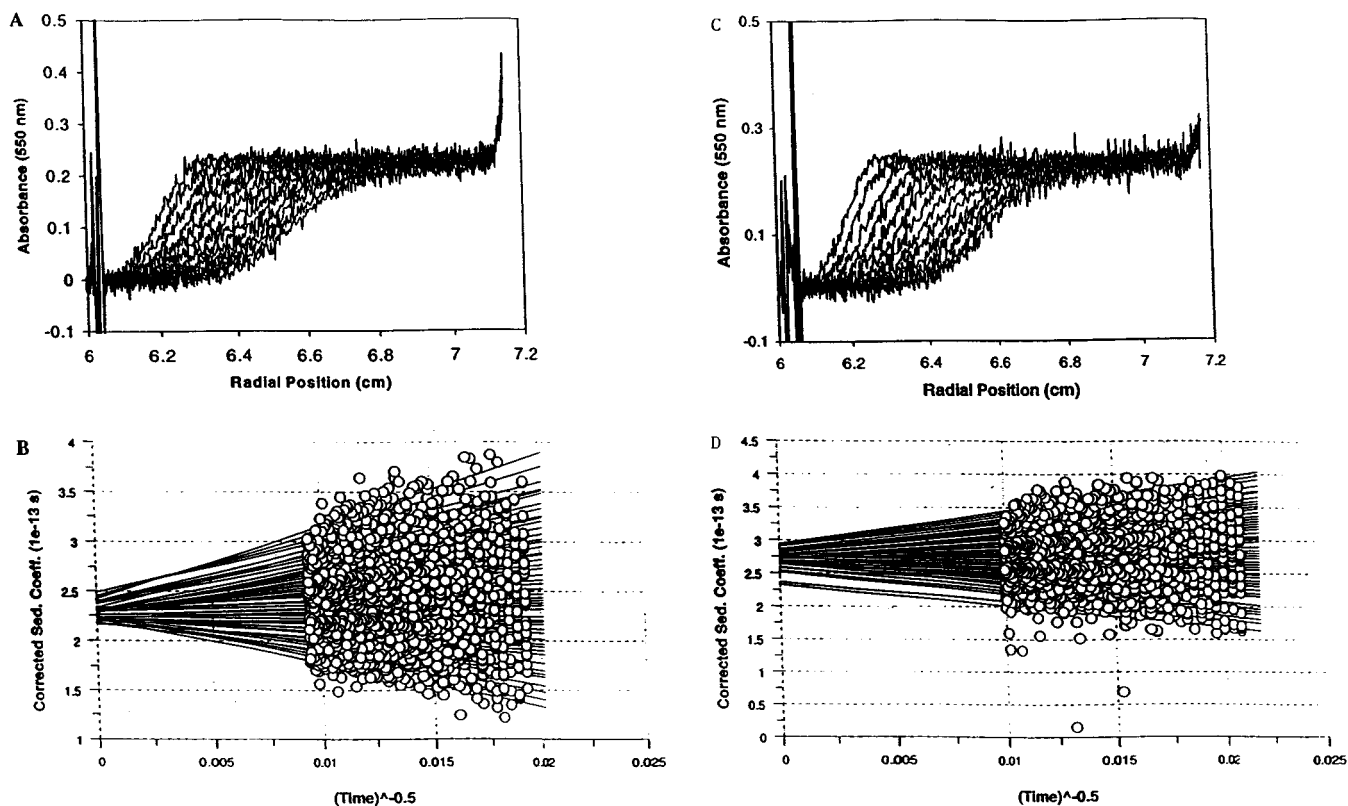
FIGURE 3: Sedimentation velocity of rhodamine-labeled gp59 (Rh-gp59) in the absence vs the presence of excess gp32 A-domain fragment. Solutions contained protein in AU-300 buffer. Settings for the analytical ultracentrifuge were as described in Experimental Procedures. (A) Sedimentation velocity boundaries obtained with Rh-gp59 alone and used in analysis by the van Holde−Weischet method. Rh-gp59 was present at an initial loading concentration of 5 μM in AU-300 buffer. (B) Extrapolation plot of data shown in panel A (Rh-gp59 alone), representing 80% of the sedimenting boundary. (C) Sedimentation velocity boundaries obtained with Rh-gp59 plus A-domain. The initial loading concentrations of Rh-gp59 and A-domain were 5 and 10 μM, respectively, in AU-300 buffer. (D) Extrapolation plot of the data shown in panel C (Rh-gp59 plus A-domain), representing 80% of the sedimenting boundary.
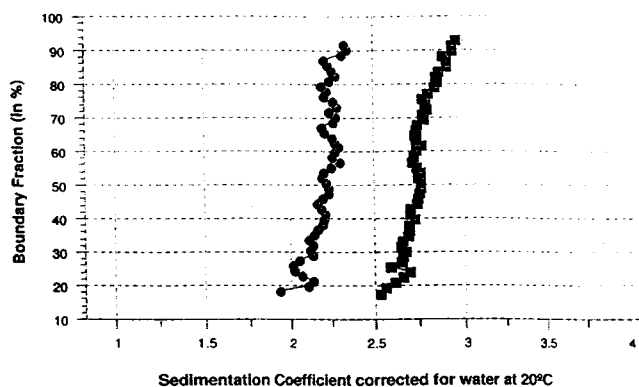

FIGURE 4: Integral distribution of $s_{20,w}$ for Rh-gp59 in the absence vs the presence of excess gp32 A-domain fragment. Data are derived from the experiments and plots represented in Figure 3. Filled circles: Rh-gp59 alone, data derived from Figure 3B. Filled squares: Rh-gp59 plus A-domain, data derived from Figure 3D.

firmed by sedimentation equilibrium data (Figure 5B), wherein the data are fit optimally by an ideal single component model yielding an apparent mass of 37.2 kDa, which is within 4.8% of the calculated mass of a heterodimeric Rh-gp59−A-domain complex (Table 1B). The ability to fit Rh-gp59−A-domain sedimentation equilibrium data by a single component model indicates that the components do not dissociate appreciably under the experimental conditions used. This is consistent with the data in Figure 2 and with our previous observation that gp59 forms a very high affinity, salt-resistant complex with the A-domain of gp32 (9).

Gp59−gp32-B complexes were investigated by sedimentation velocity employing the time derivative method of Stafford (24). As shown in Table 1A, gp59 and gp32-B have nearly identical $s_{20,w}$ values; therefore, these species are not resolvable by this method. However, if the two proteins interact to form a discrete complex with a higher $s_{20,w}$ value, then this faster sedimenting species should be resolvable from its free components by sedimentation velocity. Figure 6A shows the $g(s^*)$ plots for samples containing three different input molar ratios of the two proteins, e.g., [gp59]:[gp32-B] = 1:4, 1:2, and 1:1. Higher [gp59]:[gp32-B] ratios were not analyzed because these samples tended to form visible precipitates (unpublished results). The data clearly show that as the [gp59]:[gp32-B] ratio increases and approaches 1:1, the $g(s^*)$ profile shifts to the right, indicative of a new, faster sedimenting species in the mixture (Figure 6A). Data in Figure 6A for the 1:1 ratio of gp59 to gp32-B were fit optimally by a two-Gaussian model, representing species with $s_{20,w}$ values of 2.5 and 3.5 S, respectively (Figure 6B, Table 1B). The 3.5S species is most likely to represent a discrete complex of gp59 and gp32-B, and its low $s_{20,w}$ value suggests an arrangement of one molecule of gp59 bound to one molecule of gp32-B, when compared to the calculated s_{max} of such a heterodimer (Table 1B). We were unable to confirm this by sedimentation equilibrium due to instability of the solutions, i.e., their tendency to precipitate over the time course of equilibrium runs (unpublished results). Nevertheless, in combination with fluorescence anisotropy data, above (Figure 2), these results argue strongly for a
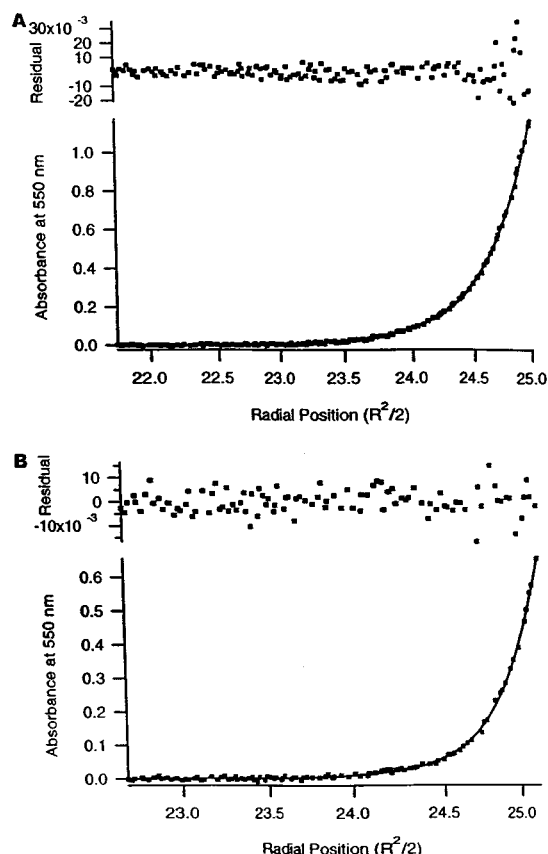
FIGURE 5: Sedimentation equilibria of Rh-gp59 in the absence vs the presence of excess gp32 A-domain fragment. Solutions contained protein in AU-300 buffer. Settings for the analytical ultracentrifuge were as described in Experimental Procedures. Absorbance data at 550 nm were collected after 24 h at 30 000 rpm, 20 °C. (A) Rh-gp59 alone, at an initial loading concentration of 4 μM. (B) Rh-gp59 plus A-domain, at initial loading concentrations of 2 and 4 μM, respectively.

bimolecular, heterodimeric gp59−gp32-B complex.

The apparent persistence of a 2.5S peak in the 1:1 gp59: gp32-B sedimentation velocity data (Figure 6B) is surprising considering the ≤ 3 nM dissociation constant estimated for the rhodamine-labeled complex in fluorescence anisotropy experiments under similar buffer conditions (Figure 2). Assuming that the 2.5S peak represents an equimolar mixture of free gp59 and free gp32-B, then the apparent dissociation constant of this complex would be on the order of 1 μM, i.e., $>10^3$-fold higher than that measured for Rh-gp59− gp32-B by fluorescence anisotropy. This seems highly unlikely given that the helicase loading activities of native and rhodamine-labeled gp59 (measured at concentrations of 100−300 nM) are virtually identical. A much more likely explanation is that the 2.5S peak in Figure 6B represents a small excess of one protein created by the selective precipitation of the other component. This is consistent with our observations that 1:1 mixtures of gp59 and gp32-B are unstable in solution during attempted sedimentation equilibrium runs and that large precipitates form at moderately higher ratios of gp59 to gp32-B during sedimentation velocity runs (unpublished results).

Hydrodynamic Shape Modeling of Gp59 and Gp59−Gp32 Complexes. Hydrodynamic shape parameters for gp59 and its complexes with A-domain and gp32-B were calculated from the sedimentation velocity data in Table 1, using the
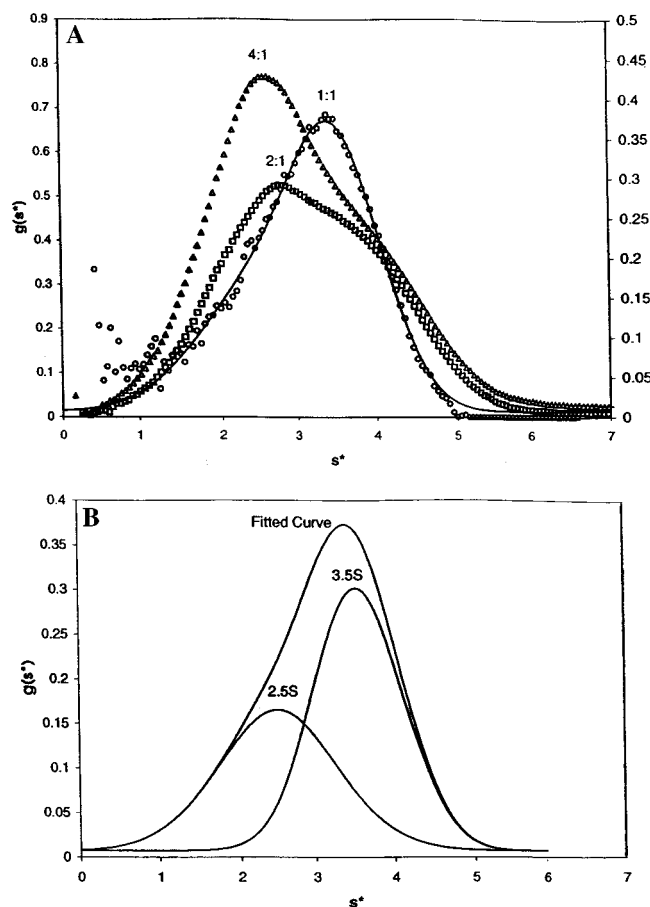

FIGURE 6: Sedimentation velocity of gp59:gp32-B mixtures. (A) Time derivative of the concentration profiles for solutions containing a 1:4 molar ratio of gp59:gp32-B, initial loading concentrations of 20 μM gp32-B and 5 μM gp59 (open triangles, plotted using the scale shown on the left-hand vertical axis); 1:2 molar ratio of gp59: gp32-B, initial loading concentrations of 10 μM gp32-B and 5 μM gp59 (open squares, plotted using the scale shown on the left-hand vertical axis); 1:1 molar ratio of gp59:gp32-B, initial loading concentrations of 5 μM gp32-B and 5 μM gp59 (open circles, plotted using the scale shown on the right-hand vertical axis). The solid line represents the two-Gaussian fit of the 1:1 gp59:gp32-B data (see panel B). All experiments were performed in AU-50 buffer, 20 °C, at a rotor speed of 60 000 rpm. Rayleigh interference data were collected and analyzed as described in Experimental Procedures. (B) Data from the 1:1 gp59:gp32-B experiment shown in panel A were fit to the sum of two Gaussian curves using IgorPro software. A two-Gaussian model was used since gp59 and gp32-B have the same $s_{20,w}$ value, equal to 2.5 S under these experimental conditions (see Table 1). Therefore, 2.5 S was held constant as the peak of one Gaussian, while the second Gaussian was fitted without restriction while minimizing differentials. This procedure resulted in a fitted $s_{20,w}$ value of 3.5 S for the gp59:gp32-B complex, and the summation of the two Gaussians described the experimental data for 1:1 gp59:gp32-B with a high degree of accuracy (see panel A).

SEDNTERP program as described in Experimental Procedures. The calculated shape parameters are listed in Table 2. For free gp59 protein, the best agreement between hydrodynamic and X-ray crystallographic data was obtained by assuming a prolate ellipsoid model. The calculated axial ratio (*a/b*) for gp59 based on hydrodynamic data is 3.1 (Table 2), which is in close agreement with the value of 2.9 measured directly from the X-ray crystal structure (7). Thus gp59 has an elongated structure in solution as well as in the crystal lattice.

Table 2: Modeled Hydrodynamic Shape Parameters of Gp59, the Gp59:A-Domain Complex, and the Gp59:Gp32-B Complex[a]

protein/complex	f/f_0[b]	a/b[c]	$2a$ (nm)[d]	$2b$ (nm)[e]	hydration expansion (%)
Rh-gp59	1.29	3.11	9.72	3.13	14.66
Rh-gp59−A-domain	1.36	3.81	12.42	3.26	15.35
gp59−gp32-B	1.45	5.09	17.71	3.48	15.53

[a] Calculated parameters are based on calculated mass, $\bar{v}$, s_{max}, and experimental $s_{20,w}$ values listed in Table 1. All calculations were performed using the program SEDNTERP, assuming a prolate ellipsoid model for each particle. [b] Relative frictional coefficient, where f_0 equals minimal frictional coefficient. [c] Maximum axial ratio. [d] Length of major hydrodynamic axis. [e] Length of minor hydodynamic axis.

Similar calculations based on sedimentation velocity data for Rh-gp59−A-domain and for gp59−gp32-B yielded axial ratios of 3.8 and 5.1, respectively, for these complexes (Table 2), assuming a prolate ellipsoid model. Thus the hydrodynamic data suggest that gp59 complexes with the two gp32 truncation derivatives are even more asymmetric than is gp59 alone. Note that in each case the model predicts an increase in the major (*a*) axis with little or no change in the minor (*b*) axis (Table 2). Thus the hydrodynamic data for gp59−gp32 sp. complexes *could* be explained by a binding site located at one end of the prolate ellipsoid gp59 molecule, which would imply that only one of gp59's two globular domains (N or C) forms contacts with the A-domain of gp32. This possibility is discussed further below.

DISCUSSION

Our major conclusions may be summarized as follows: (1) T4 helicase assembly protein gp59 forms stable ($K_d \leq$ 2−3 nM) heterodimers with fragments of the gp32 ssb protein containing the A-domain. Thus the fundamental interaction between gp59 and gp32 in the T4 replication system involves a 1:1 association of a gp32 molecule's A-domain with a molecule of gp59. This 1:1 association is independent of gp32's core (ssDNA binding) domain since nearly identical gp59 binding stoichiometries and affinities are estimated with the A-domain fragment alone and with gp32-B, which contains both A-domain and core domain. (2) Changes in the fluorescence anisotropy of rhodamine-labeled gp59 (Rh-gp59) indicate that this protein undergoes a conformational change upon contact with gp32's A-domain, consistent with observations that A-domain binding attenuates DNA binding activities of gp59 (*10*; T. Wang and S. Morrical, manuscript in preparation). (3) Predictions of the hydrodynamic shapes of gp59−gp32 derivative heterodimers may imply that the A-domain contacts a single domain of gp59 (either its N- or C-domain) along the major axis of a gp59 structure that is roughly prolate ellipsoid in shape.

Our observation that gp59 forms 1:1 complexes with gp32 derivatives is consistent with the previous finding that gp59 and gp32 exhibit similar ssDNA binding site sizes ($n = 7−10$ nucleotide residues per gp32 molecule and $n = 9−10$ nucleotide residues per gp59 molecule; *8, 31*), arguing that a 1:1 gp59:gp32 binding stoichiometry is likely to be conserved locally within the tripartite gp59−gp32−ssDNA complex which is the loading target for the T4 replicative DNA helicase, gp41. This argument is supported by the observation that ssDNA−cellulose affinity resin saturated

with gp32 is capable of retaining an amount of gp59 that is approximately equimolar to the bound gp32 (*9, 10*). These and other data strongly suggest that the repeating unit of the helicase loading target in T4 replication may be a gp59−:gp32 heterodimer bound to 7−10 nucleotides of ssDNA. This raises the obvious question of how many repeating units are necessary for helicase loading. Previous studies investigating helicase loading onto ssDNA molecules coated with different molar ratios of gp32 and gp32-A (a form of gp32 lacking the A-domain and therefore incapable of productive binding to gp59) suggested that at least three intact gp32 molecules bound contiguously to ssDNA constitute the minimal site for gp59-directed assembly of the gp41 DNA helicase (*9*). This would imply a minimum cluster of at least three gp59−gp32 units bound to at least 21−30 nucleotides of ssDNA required for helicase assembly. In comparison, the binding site size of one *monomer* of the gp41 helicase on ssDNA has been estimated to be 12−20 nucleotide residues (*32*); therefore, the proposed minimum helicase target covers sufficient ssDNA to provide a nucleation site for helicase binding.

The requirement for a cluster of gp59 and gp32 molecules bound to ssDNA may provide a role for gp59 cooperativity in the helicase assembly process. Gp59−ssDNA interactions exhibit at least two different modes of cooperativity, including a high cooperativity mode ($\omega \approx 2500$) observed under some conditions in vitro (*8*). Highly cooperative binding of gp59 to a gp32−ssDNA complex would allow the clustering of gp59 and gp32 molecules necessary to reconstitute a helicase assembly site, even at the relatively low concentrations of gp59 believed to prevail during T4 infection (see ref *33*). Given the demonstrated affinity of gp59 for replication fork DNA (*7*), it is interesting to speculate that an initial gp59 binding event at a replication fork would quickly lead to cluster formation as gp59 binding propagates onto the gp32-covered ssDNA of the lagging strand template. However, the mechanism of delivery of gp59 to the replication fork depends greatly upon its associative state prior to ssDNA binding. We have estimated upper limit dissociation constants for the gp59−gp32-B and gp59−A-domain complexes in the low nanomolar range (see Figure 2 and related text). Assuming a similar K_d for the complex of native gp32 with gp59, as appears likely from competition data (unpublished results), then we would predict that the latter exists exclusively in the gp32-bound form on the basis of the abundance of gp32 throughout all but the earliest, prereplicative stages of T4 infection in *E. coli* (estimated 10 000 gp32 molecules per cell or 30−40 μM intracellular concentration; see ref *33*) and on an estimated intracellular gp59 concentration in the mid-nanomolar range. Furthermore, since interaction with the A-domain of gp32 attenuates the observed ssDNA binding affinity of gp59 (*10*), it seems likely that gp32, not DNA, is the primary binding target of gp59 in vivo. Thus gp59-complexed gp32 may constitute a unique subpool of the overall gp32 pool in the T4-infected cell. Hence the mechanism of gp59 delivery to the replication fork most consistent with the available data would appear to be one in which both members of a preexisting gp59−gp32 complex bind to the ssDNA as it is exposed by replication fork movement.

And what is the nature of this complex? While we have demonstrated that truncated forms of gp32 containing the

A-domain form heterodimers with gp59, it is probable that intact gp32 molecules capable of undergoing self-association form higher order mixed oligomers with gp59. Our data plus previously published results (*9, 10*) argue that the 1:1 stoichiometric relationship between gp59 and gp32 is likely to be preserved within these mixed oligomers. How then is gp59 targeted to the replication fork? An intriguing possibility is the following: the gp59−gp32 oligomers form in solution and then bind as a unit to the exposed lagging strand ssDNA, adding onto the 5′ end of a growing gp32−ssDNA cluster. Recruitment of the gp59−gp32 oligomer to the fork could be enhanced by gp59−fork DNA interactions (*7, 13*).

Our sedimentation data confirm the essentially monomeric structure of free gp59 in solution, consistent with this protein's X-ray structure and with results from density gradients (*5, 7*). This property is somewhat surprising given the cooperative nature of gp59−ssDNA interactions (*8*), the propensity of gp59 to form condensed clusters with gp32 on ssDNA (*10*), and indirect data suggesting that gp59 and gp41 helicase may function together as a 6:6 complex (*6, 13*), all of which suggest that oligomer formation may be an important property of gp59. It appears very likely that heteroassociations with DNA, gp32, and/or gp41 are necessary to stabilize gp59 oligomers. However, the ability of gp59 molecules to be cross-linked to each other in the presence of a thiol-selective cross-linking reagent (*34*) and to form intermolecular disulfide bridges during labeling with 5-TM-RIA (Figure 1) indicates that gp59 monomers may oligomerize transiently in the absence of other macromolecules.

The X-ray crystallographic structure of gp59 reveals an asymmetric, predominantly α-helical molecule comprised of two distinct domains, designated the N- and C-domains for their proximity to the N- and C-termini of the protein, respectively (*7*). The X-ray structure of gp59 is elongated and roughly prolate ellipsoidal in shape, with an axial ratio of approximately 3, and with the centers of the N- and C-domains lying roughly along the major axis. Our sedimentation velocity data are consistent with an overall increase in asymmetry upon formation of gp59−A-domain and gp59−gp32-B complexes. As shown by a computer model, the increase in asymmetry can be explained by complexes that extend the major prolate axis with little or no change in the minor axis (Table 2). This model predicts that the A-domain of gp32 must contact either the N- or the C-domain of gp59 to form a more elongated complex. Consistent with this prediction, Benkovic and co-workers propose a model in which the A-domain of gp32 forms an extensive interface with the C-domain of gp59 (*34*). However, chemical cross-linking data indicate that further interactions occur between the core domain of gp32 and the N-domain of gp59 (*34*), a finding that in its simplest interpretation appears inconsistent with the hydrodynamic model of the gp59−gp32-B complex described in Table 2. Both hydrodynamic and cross-linking data appear to conflict with the model of Mueser et al. of gp59 and gp32 arrangement on fork DNA (*7*), which places gp32's A-domain in contact with the N-domain of gp59 and in an orientation that would substantially increase the minor prolate axis. Of course, it is quite possible that the presence of ssDNA and/or the B-domain of gp32 could affect the orientation of domains and overall shape of the complex. Further experimentation is clearly needed to ascertain the actual distribution and extent of gp59−gp32 binding surfaces.

Our observation that the binding of gp32-B and A-domain fragments causes similar *decreases* in the fluorescence anisotropy of rhodamine-labeled gp59 indicates that these gp32 derivatives induce a similar conformational change in gp59, one resulting in increased mobility of at least one rhodamine moiety conjugated to gp59. We hypothesize that gp32 derivative binding causes an increase in the mobility of rhodamine conjugated to Cys42, the cysteine most likely to be fully labeled based upon its accessibility to solvent in the gp59 X-ray structure (*7*). This residue lies in a loop between α-helices H1 and H2, which forms part of the solvent-exposed surface of the HMG-like N-domain of gp59. Loop H1−H2 is layered against core helices of the N-domain and is stabilized by interactions including the stacking of loop residue Trp41 against core residue Pro7. Since the N-domain including loop H1−H2 is postulated to play an important role in gp59−DNA contacts, it is reasonable to speculate that the conformation of this loop would be affected by the binding of ligands (gp32 in this instance) that modulate gp59−DNA interactions. We showed previously that binding of gp32's A-domain to gp59 strongly decreases the latter's affinity for ssDNA (*10*), and we have observed a similar effect of A-domain on gp59 interactions with fork DNA (T. Wang and S. Morrical, manuscript in preparation). Thus, the fluorescence anisotropy effects we observe with Rh-gp59 may prove to be a convenient reporter on gp59 conformational changes that affect its DNA binding properties and on the protein interactions that mediate these changes.

REFERENCES

1. Dong, F., Gogol, E. P., and von Hippel, P. H. (1995) *J. Biol. Chem. 270*, 7462−7473.
2. Nossal, N. G. (1994) in *Molecular Biology of Bacteriophage T4* (Karam, J. D., Ed.) pp 43−53, American Society for Microbiology, Washington, DC.
3. Barry, J. E., and Alberts, B. M. (1994) *J. Biol. Chem. 269*, 33049−33062.
4. Beernink, H. T. H., and Morrical, S. W. (1999) *Trends Biochem. Sci. 24*, 385−389.
5. Yonesaki, T. (1994) *J. Biol. Chem. 269*, 1284−1289.
6. Morrical, S. W., Hempstead, K., and Morrical, M. D. (1994) *J. Biol. Chem. 269*, 33069−33081.
7. Mueser, T. C., Jones, C. E., Nossal, N. G., and Hyde, C. C. (2000) *J. Mol. Biol. 296*, 597−612.
8. Lefebvre, S. L., and Morrical, S. W. (1997) *J. Mol. Biol. 272*, 312−326.
9. Morrical, S. W., Beernink, H. T. H., Dash, A., and Hempstead, K. (1996) *J. Biol. Chem. 271*, 20198−20207.

10. Lefebvre, S. D., Wong, M. L., and Morrical, S. W. (1999) *J. Biol. Chem. 274*, 22830−22838.

11. Tarumi, K., and Yonesaki, T. (1995) *J. Biol. Chem. 270*, 2614−2619.

12. Raney, K. D., Carver, T. E., and Benkovic, S. J. (1996) *J. Biol. Chem. 271*, 14074−14081.

13. Jones, C. E., Mueser, T. C., and Nossal, N. G. (2000) *J. Biol. Chem. 275*, 27145−27154.

14. Kreuzer, K. N., and Morrical, S. W. (1994) in *Molecular Biology of Bacteriophage T4* (Karam, J. D., Ed.) American Society for Microbiology, pp 28−42, Washington, DC.

15. Kreuzer, K. N. (2000) *Trends Biochem. Sci. 25*, 165−173.

16. Formosa, T., and Alberts, B. M. (1986) *Cell 47*, 793−806.

17. Bleuit, J. S., Xu, H., Ma, Y., Wang, T., Liu, J., and Morrical, S. W. (2001) *Proc. Natl. Acad. Sci. U.S.A*. (in press).

18. Williams, K. R., Shamoo, Y., Spicer, E. K., Coleman, J. E., and Konigsberg, W. H. (1994) in *Molecular Biology of Bacteriophage T4* (Karam, J. D., Ed.) American Society for Microbiology, pp 301−304, Washington, DC.

19. Spacciapoli, P., and Nossal, N. G. (1994) *J. Biol. Chem. 269*, 447−455.

20. Giedroc, D. P., Khan, R., and Barnhart, K. (1990) *J. Biol. Chem. 265*, 11444−11455.

21. Hurley, J. M., Chervitz, S. A., Jarvis, T. C., Singer, B. S., and Gold, L. (1993) *J. Mol. Biol. 229*, 398−418.

22. Gill, S. C., and von Hippel, P. H. (1989) *Anal. Biochem. 182*, 319−326.

23. Kopelman, M., Cogan, U., Mokady, S., and Shinitzky, M. (1976) *Biochim. Biophys. Acta 439*, 449−460.

24. van Holde, K. E., and Weischet, W. O. (1978) *Biopolymers 17*, 1387−1403.

25. Stafford, W. F. (1992) *Anal. Biochem. 203*, 295−301.

26. Yphantis, D. A. (1964) *Biochemistry 3*, 297−317.

27. Laue, T. M., Shah, B. D., Ridgeway, T. M., and Pelletier, S. L. (1992) in *Analytical Ultracentrifugation in Biochemistry and Polymer Science* (Harding, S. E., et al., Eds.) pp 90−125, Royal Society of Chemistry, Cambridge, U.K.

28. Teller, D. C. (1976) *Nature 260*, 729−731.

29. Chase, J. W., and Williams, K. R. (1986) *Annu. Rev. Biochem. 55*, 103−136.

30. Karpel, R. L. (1990) in *The Biology of Nonspecific DNA Protein Interactions* (Revzin, A., Ed.) pp 103−130, CRC Press, Boca Raton, FL.

31. Kowalczykowski, S. C. (1990) in *Landolt-Bornstein: Numerical Data and Functional Relationships in Science and Technology* (*New Series*). *Group VII: Biophysics, Nucleic Acids, 1d* (Saenger, W., Ed.) pp 244−263, Springer-Verlag, Berlin.

32. Young, M. C., Schultz, D. E., Ring, D., and von Hippel, P. H. (1994) *J. Mol. Biol. 235*, 1447−1458.

33. Cowan, J., D'Acci, K., Guttman, B., and Kutter, E. (1994) in *Molecular Biology of Bacteriophage T4* (Karam, J. D., Ed.) pp 520−527, American Society for Microbiology, Washington, DC.

34. Ishmael, F. T., Alley, S. C., and Benkovic, S. J. (2001) *J. Biol. Chem.* (in press).